Materials Advances

ROYAL SOCIETY OF CHEMISTRY

PAPER

View Article Online
View Journal | View Issue

Cite this: *Mater. Adv.*, 2024, 5, 349

Unveiling the role of electrode polarization in modulating dielectric and electro-optical properties of SnSe dispersed nematic liquid crystal†

Bhupendra Pratap Singh,[a] Piyush Mishra,[b] Mohammad Rafe Hatshan,[c] Dharmendra Pratap Singh[d] and Shug-June Hwang *[a]

This study examines the influence of SnSe nanospheres (NSs) on the dielectric and electro-optical properties of liquid crystal (LC) blends. A notable Debye relaxation phenomenon has been observed within a few Hz to near kHz frequency regime. This phenomenon is ascribed to the accumulation of mobile charge carriers near the cell electrodes (electrode polarization). We engage in a comprehensive analysis of the implications of this phenomenon on the electro-optical response, taking into account crucial factors including threshold voltage, response time, and dielectric permittivity. Our findings unveil a significant alteration in the electro-optical behavior resulting from the introduction of NSs, extending well beyond the instance of electrode polarization, although with a detrimental impact on performance within the low-frequency range. Furthermore, the inclusion of SnSe NSs within LC molecules has the potential to capture charged ionic impurities, leading to suppression of the screening effect. This, in turn, gives rise to an intensified electric field and heightened van der Waals dispersion interaction between LC molecules and alignment layers. Through COMSOL Multiphysics software simulation and experimental validation, we establish a consistency between the predicted phenomena and observed experimental results. Notably, LC cells containing 0.5 wt% SnSe NSs demonstrated superior electro-optical properties. These enhancements comprised an elevated dielectric anisotropy (increased from 14.27 to 19.50), a lowered low threshold voltage (decreased from 1.08 to 0.73 V), and a quicker response time (reduced from 11.5 to 4.01 ms), above the onset frequency of electrode polarization.

Received 27th September 2023,
Accepted 22nd November 2023

DOI: 10.1039/d3ma00769c

rsc.li/materials-advances

I. Introduction

The introduction of various nanomaterials into liquid crystals (LCs) allows the modification and imposition of distinct physical properties onto the resulting liquid crystal (LC)-nanomaterial composites. This is achieved through the synergistic coupling of the LCs' long-range ordering capabilities and the specific characteristics exhibited by the dopant nanomaterials. By strategically doping of different types of nanomaterials into LCs, it is possible to manipulate the physical behaviour of the composite materials, enabling the realization of unique and desired properties.[1] Metal, ferroelectric, semiconductor and carbon-based nanoparticles are the primary nanomaterials utilized as dopants in the LCs. Through the careful selection of dopants and the consideration of their physical and chemical attributes, along with the interactions between the LCs and nanomaterials, it is easier to achieve enhanced physical properties for exploring novel applications within these dispersions.

A prominent instance is the ability of the nematic LC phase to extend its extensive orientational order through the incorporation of nanoparticles, encompassing carbon nanotubes, nanorods, and quantum dots.[2–4] Furthermore, integrating ferroelectric nanoparticles (NPs) into LC media can confer soft memory functionalities and elevate the electro-optical responsiveness.[5–7] Various researchers have found different mesophases and different guest–host composite systems suitable for these applications.[8–12] Basu *et al.*[13] demonstrated that 5CB/BCP functionalized $BaTiO_3$ samples yield a substantial enhancement in the soft-memory effect within the isotropic phase. In a study conducted by Garbovskiy *et al.*,[14] it was demonstrated that the dispersion of nanoparticles

[a] *Department of Electro-Optical Engineering, National United University, Miao-Li-360, Taiwan. E-mail: june@nuu.edu.tw*
[b] *CSIR-National Physical Laboratory, Dr K.S. Krishnan Marg, New Delhi-110012, India*
[c] *Department of Chemistry, College of Science, King Saud University, Riyadh, 11451, Saudi Arabia*
[d] *Université du Littoral Côte d'Opale, UR 4476, UDSMM, Unité de Dynamique et Structure des Matériaux Moléculaires, Calais 62228, France*

† Electronic supplementary information (ESI) available. See DOI: https://doi.org/10.1039/d3ma00769c

within LCs can exert an impact on the concentration of mobile ions *via* temperature-dependent ion adsorption and desorption processes. Another research study by Rivas *et al.*[15] involved the design, fabrication, and measurement of a device comprising an array of aluminium NPs covered by a nematic liquid crystal (NLC). This device demonstrated the capability to manipulate the energy of a surface lattice resonance (SLR) by altering the refractive index of the LC through the application of an electric potential. Yamamoto *et al.*[16] examined liquid crystalline 2D borophene oxide for use in inorganic optical devices. Several investigations have found that inorganic nano-additives inhibit mobile ions in LC cells.[17–19] The dispersion of semiconductor NPs in the nematic LCs has emerged as a captivating research area, primarily due to its promising applications in optoelectronics and display technologies.[17,20–23] Semiconductor NPs exhibit distinct optical and electrical properties, while nematic LCs offer anisotropic molecular ordering and responsiveness to an external stimuli.[23] The integration of these materials has the potential to unlock new functionalities and enhance the performance of devices.[24–26] Furthermore, the inclusion of semiconductor NPs can introduce novel optical properties, including enhanced absorption or emission characteristics that can be used in displays, sensors, and photovoltaic devices.[27–29] Moreover, the anisotropic nature of the LCs allows for precise control over the alignment of the nanoparticles, leading to tunable optical properties based on their orientation. This tunability is particularly valuable for tunable filters or polarizers, where the ability to manipulate the optical properties of the composite material is crucial for optimal device performance.[30,31] Nevertheless, doping with NPs can potentially result in aggregation of the particles. The presence of particle aggregation can have both pros and cons on the LC system. On one hand, it may be beneficial as it can reduce the viscosity of the LC by providing an additional shear-drift to the LC molecules to move more freely.[5,32,33] On the other hand, particle aggregation can also have detrimental effects, such as the degradation of the LC's elastic properties or an induction of light scattering phenomena.[34] In order to achieve the desired properties of the suspension, it is imperative to have a comprehensive understanding and precise control over these contrasting effects.

Tin-mono-selenide (SnSe) stands as a semiconductor chalcogenide material that has garnered considerable attention in contemporary times due to its unique attributes and potential applications in electronics, optoelectronics, and energy storage. Notably, SnSe manifests both direct and indirect band gaps, with a direct band gap measuring 0.9 eV and an indirect band gap measuring 1.3 eV.[35,36] It is commonly a p-type semiconductor, with hole concentrations ranging from 10^{17} to 10^{18} cm^{-3} and room temperature electric resistance ranging from 10^{1} to 10^{5} Ω cm^{-1}.[37] Due to its unique 2D layered structure and favourable optoelectronic properties, SnSe has been utilized for field emission applications.[35,36] It is particularly attractive for applications in photovoltaics and optoelectronics as well.[35,38]

Exploration into SnSe single crystals has centered around their potential as thermoelectric materials, revealing an impressive figure of merit (ZT) value of 2.6, underscoring their remarkable thermoelectric efficiency.[39] Lately, researchers have made significant progress in enhancing the field emission characteristics of SnSe by modifying its structural and surface morphologies, specifically by developing SnSe nanoflowers.[40] These modifications have resulted in significantly improved field emission properties.

Field electron emission is the mechanism responsible for field emission in semiconducting nanoparticles such as SnSe. It involves the emission of electrons from the nanoparticle surface under the influence of a high electric field (~ 2 V μm^{-1}). This electric field surpasses the potential barrier at the material's surface, enabling electrons to tunnel out and escape into vacuum or the surrounding medium. The field emission characteristics of SnSe semiconducting NPs can be attributed to several factors. Firstly, these NPs typically possess a low work function, which represents the energy required to remove an electron from their surface. This low work function facilitates the emission of electrons under an applied electric field. Secondly, the nanoscale dimensions of SnSe NPs result in a high surface-to-volume ratio, creating numerous emission sites. This increased surface area promotes electron emission and contributes to the overall field emission behavior. Moreover, SnSe NPs exhibit the quantum confinement effect, where the electronic properties are modified due to the confinement of charge carriers within a small volume. This confinement effect enhances the field emission characteristics compared to bulk materials. Field emission from SnSe NPs has applications in various areas, including electron sources for vacuum microelectronics, field emission displays, electron microscopy, gas sensors and energy harvesting devices.[40] While electron emission from material surfaces has been extensively studied to obtain a fundamental understanding, it also has significant potential for a wide range of practical applications. These applications include, but are not limited to, telecommunication satellites, medical devices, space research, X-ray sources, and electronic displays. The ability to harness electron emission from material surfaces has opened up avenues for advancements in various fields, making it an area of great importance and interest.

Herein, we have examined the effects of doping E7 nematic LCs (NLCs) with SnSe nanospheres (NSs). SnSe NSs exhibit an orthorhombic structure and the *Pnma* (No. 62) space group and have not yet been used so far to improve the properties of NLCs. This study investigated the influence of SnSe NSs on the dielectric and electro-optical properties of a nematic LC. The crystal rotation method confirms the improvement of pretilt angle and alignment of the LC molecules within the SnSe-dispersed LC cells. The SnSe-dispersed LC cell exhibits several advantages, including a lower threshold voltage, enhanced dielectric permittivity and anisotropy, reduced operational voltage, lower rotational viscosity, and faster response time. The dielectric data of pristine and SnSe-dispersed LC cells under homogeneously aligned (HA) and vertically aligned (VA) LC cells have been fitted *via* Cole–Cole theory, enabling the calculation and analysis of the dielectric strength and relaxation frequency of the E7/SnSe NSs dispersed systems. Notably, the dispersion of SnSe NSs significantly enhances the dielectric strength of the E7/SnSe dispersed systems. The behaviour of composite systems has been explained in light of guest–host interactions between the E7 NLC and SnSe NSs.

II. Experimental details

2.1. Chemical synthesis of tin-mono-selenide (SnSe) nanospheres

The following provides a detailed procedure for the synthesis of SnSe NSs using the hot-injection colloidal synthesis method.[38] To maintain an inert atmosphere, the synthesis process was carried out in a nitrogen glove box. Firstly, 1.1 g of elemental Se was dissolved in 14 mL of tri-octyl-phosphine (TOP) and stirred overnight to form a 1 M TOP/Se solution. Subsequently, 14 g of oleylamine was placed in a three-neck flask, which was connected to a Schlenk line. The flask was heated to 105 °C and purged with nitrogen for 30 minutes. Subsequently, a 2 mL portion of the TOP/Se solution was introduced into the flask under exclusion of air. The ensuing reaction mixture was then subjected to heating at the preferred temperature, typically within the range of 80 °C to 200 °C.

To prepare the tin precursor, bis(bis[trimethylsilyl]amino)-tin(II), 780 μL of the precursor was mixed with 6 mL of oleylaSmine in the nitrogen glove box. Subsequently, 6.5 mL of this solution was rapidly injected into the reaction mixture while ensuring vigorous stirring. After a duration of 15 seconds, 3 mL of oleic acid was injected into the mixture. The resulting particle suspension was further heated close to the reaction temperature and stirred for an additional 2 minutes. Finally, the particle suspension was quenched in a water bath and subjected to 5 rounds of cleaning using hexane as the solvent and isopropanol as the antisolvent.

2.2. Host nematic liquid crystal (NLC)

The host nematic LC mixture E7 (Daily Polymer Kaohsiung, Taiwan), utilized in the current study, exhibited a nematic–isotropic phase transition temperature of 61 °C, an optical anisotropy *i.e.*, birefringence ($\Delta n = n_e - n_o$) of 0.2246 (n_o = 1.5216 and n_e = 1.7462) at 589 nm, and a dielectric anisotropy ($\Delta\varepsilon = \varepsilon_{\parallel} - \varepsilon_{\perp}$) of 14.1 ($\varepsilon_{\parallel}$ = 19 and $\varepsilon_{\perp}$ = 4.9) at 1 kHz at room temperature (RT). The LC mixture was first heated to an isotropic phase before being injected through the self-assembled 5.2 μm empty cell *via* capillary action.

2.3. Measurement techniques

We unveil a new basic framework for designing the optical and alignment properties of SnSe in a nematic NLC host with experimental data from the system under consideration. The dielectric measuring sample holders were home-built from indium–tin-oxide (ITO) coated glass substrates and the fabrication details of these sample holders are provided in our articles published previously.[17,41] Optical interferometry was employed for the confirmation of thickness of these sample cells, which was found to be ~5.2 ± 0.05 μm.[42] LC/SnSe mixtures were prepared with concentrations of NSs fixed to 0.01, 0.05, 0.1, 0.3 and 0.5 wt% into E7 NLC. These mixtures were heated above isotropic temperature and filled uniformly into these sample holders *via* capillary action, after which they were cooled down at a slow rate.

The dimensions and shape of nanospheres (NSs) were determined using scanning electron microscopy (SEM) on a Bruker QUANTAX 800 device. A small **number** of nanoparticles were directly deposited on carbon tape for this investigation. An investigation into X-ray diffraction (XRD) profiles was conducted using a Rigaku Miniflex 600 X-ray diffractometer. The examination took place under well-defined parameters, with the control voltage configured to 20 kV in the XG operational mode and a tube current of 2 mA. Utilizing CuKα radiation featuring a wavelength of 1.54 Å, the analysis encompassed a scanning step size of 0.02°. The XRD experiments covered a glancing angle range from 20° to 80°. Additional information about the experimental techniques is described in the measurement method section of the ESI.†

Using the crystal rotating approach,[43] we also obtained the pre-tilt angles of the NLC cells with pure LC and SnSe dispersed LC. This method entailed measuring transmittance while the cells were rotated latitudinally by ±80° at room temperature, taking into account both horizontal and vertical cell arrangements. Table 1 shows the obtained pre-tilt angle values for each configuration and LC composition.

Using high electric field techniques, we computed the polar anchoring energy coefficients (W_{polar}) of pure E7 and SnSe-blended LC cells.[44] As shown in Table 1, our investigation demonstrated a small rise in the W_{polar} values for the SnSe-doped LC cells.

III. Results and discussion

Fig. 1(a) displays the scanning electron microscopic (SEM) image, utilized for analyzing the structural and morphological characteristics of SnSe nanospheres (NSs). The SEM image clearly demonstrates that the SnSe NSs have a spherical shape with a uniform size distribution ranging from 40 to 75 nm.

To investigate the structural properties of SnSe nanospheres (NSs), powder X-ray diffraction was performed, and the corresponding XRD pattern is presented in Fig. 1(b). The XRD pattern confirms the crystalline nature of SnSe. Notably, the diffraction peaks observed at 2θ = 31.80° (210), 33.13° (201), 38.34° (011), 37.02° (111), 39.07° (400), 47.81° (311), 55.14° (020), 63.53°

Table 1 Pre-tilt angles and polar anchoring energies of homogeneously and vertically aligned LC cells, and pure and SnSe blended LC cells at room temperature

Concentration of SnSe NSs (wt%)	0.00	0.01	0.05	0.1	0.3	0.5
Pre-tilt angle of HA cell (Degrees)	2.75	2.56	2.22	2.10	1.96	1.65
Pre-tilt angle of VA cell (Degrees)	88.50	88.76	88.81	88.89	88.95	89.16
$W_{polar}^{Experimental}$ (10^{-4} J m^{-2})	2.66	2.81	2.93	3.22	3.44	3.65
$W_{polar}^{Theoretical}$ (10^{-4} J m^{-2})	2.75	2.92	3.02	3.35	3.50	3.75

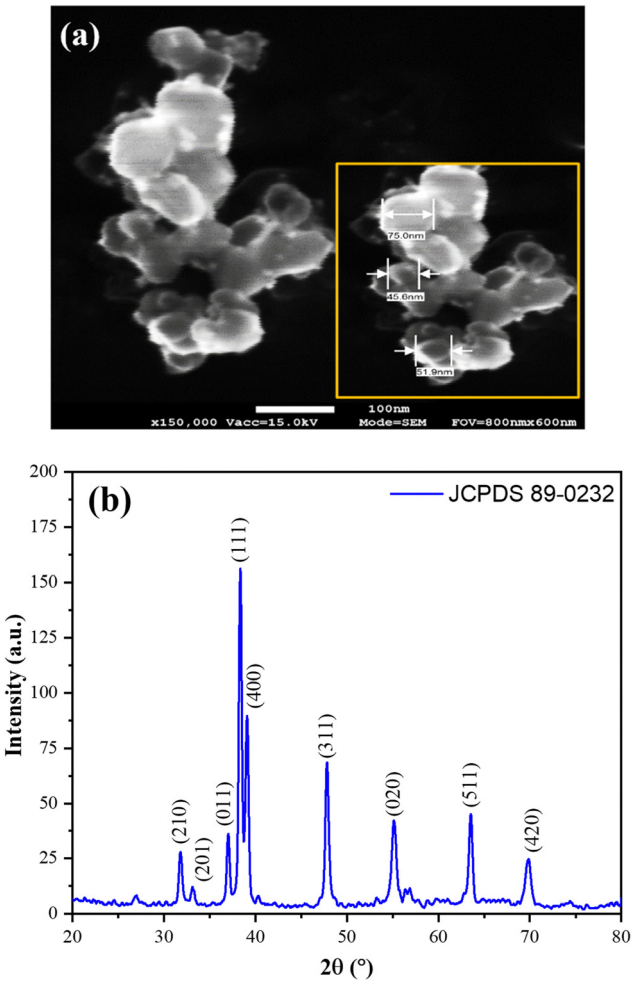

Fig. 1 (a) Scanning electron microscopic (SEM) image and (b) X-ray diffraction (XRD) spectrum of the SnSe NSs. The inset of (a) represents the enlarged view with the size estimation of SnSe NSs.

(511), and 69.81° (420) match well with JCPDS 89-0232, confirming the orthorhombic phase of SnSe.

To determine the average crystallite size of grains (D), the Debye–Scherrer formula was employed: $D = K\lambda/\beta\cos\theta$. Here, λ represents the X-ray wavelength, K denotes the Scherrer constant (approximately 0.98), β corresponds to the broadening at half the maximum intensity (FWHM) measured in radians, and θ indicates the Bragg angle. The calculated average crystallite size was found to be approximately 23.8 nm, corresponding to the (420) crystal plane.

The alignment properties of a liquid crystal (LC) cell containing pure E7 as well as five different concentrations of SnSe nanospheres (NSs) were investigated using a crossed-polarized optical microscope (POM). The LC cells were homogeneously aligned (HA) and had a thickness of 5.2 μm. The rubbing directions of the cells were set at a 45° angle with respect to the transmission axis of the crossed polarizers. The POM micrographs in Fig. 2(a)(i)–(vi) show the LC texture in the bright state. These micrographs indicate uniform colors across the active area of the cells, suggesting that the SnSe NSs were evenly dispersed in the LC matrix without any noticeable aggregations. This uniformity in color persisted even after subjecting the cells to multiple cycles of voltage and temperature treatments. Furthermore, the addition of SnSe NSs resulted in a slight color shift in the micrographs, which can be attributed to a change in the birefringence (Δn) of the LC mixture. This observation indicates that the introduction of SnSe NSs influenced the optical properties of the LC cell, leading to measurable changes in color due to the modified birefringence.

Fig. 2(b) illustrates the transmission spectra of LC cells containing pure E7 and a blend of E7 and SnSe in the visible range from 400 to 700 nm. The introduction of SnSe led to changes in the refractive index of the LC mixture, causing an increase in the mismatch and haziness between the glass substrates and the LC layer. This alteration resulted in a light loss of approximately 9%, reducing the transmission from 87% to 78%. In Fig. 2(c), the voltage-dependent transmission (V–T) curves of pure E7 and SnSe-doped LC cells are presented at room temperature. Notably, with an increase in the concentration of the SnSe dopant, the V–T curve exhibited a slight shift towards the low-voltage region. This shift signifies that even a small quantity of SnSe nanoparticles (NPs) can notably lower the threshold and operational voltage of the E7/SnSe composite.

The changes in transmission observed in the V–T curve are closely related to the fluctuations in phase retardation, as described by eqn (1):[45]

$$T_r = \sin^2 2\theta \sin^2\left(\frac{\delta}{2}\right), \quad (1)$$

where, T_r, θ and δ represents the transmission, the angle between transmission axis of the polarizer and rubbing direction, and the phase retardation respectively. eqn (1) states that once δ reaches an even multiple of π, the T_r of the V–T curve will be zero as indicated in Fig. 2(c). The LC exhibited Fréedericksz transition characteristics in the nematic phase. When an external electric field ($\vec{E}$) is applied across the LC cell, LC molecules undergo reorientation due to a rotational torque ($\tau \propto \Delta\varepsilon E^2$) leading to rotation of the nematic director from a homogeneous to a homeotropic configuration. The overall orientational order of the nematic phase is vanished at the nematic–isotropic phase transition temperature (T_{NI}), at which Fréedericksz transitional phenomenon no longer exist. The significant shift of the V–T curve towards lower voltage, indicating the small amount of SnSe NSs can significantly reduce the Fréedericksz transition voltage or threshold voltage (V_{th}) and operating voltage (V_{op}) of the blended LC cells (see Table 2).

In this study, we have employed two techniques to investigate the relationship between the SnSe concentration in E7 and the threshold voltage: the V–T curve method and the POM experimental technique. In the V–T curve approach, V_{th} was determined as the initial transmission begins to change. Conversely, the POM technique relied on identifying the voltage at which the color of the POM image exhibited initial alterations, indicating the onset of distortion in the liquid crystals (LCs). These techniques allowed for the acquisition of two independent characteristics associated with the threshold voltage.

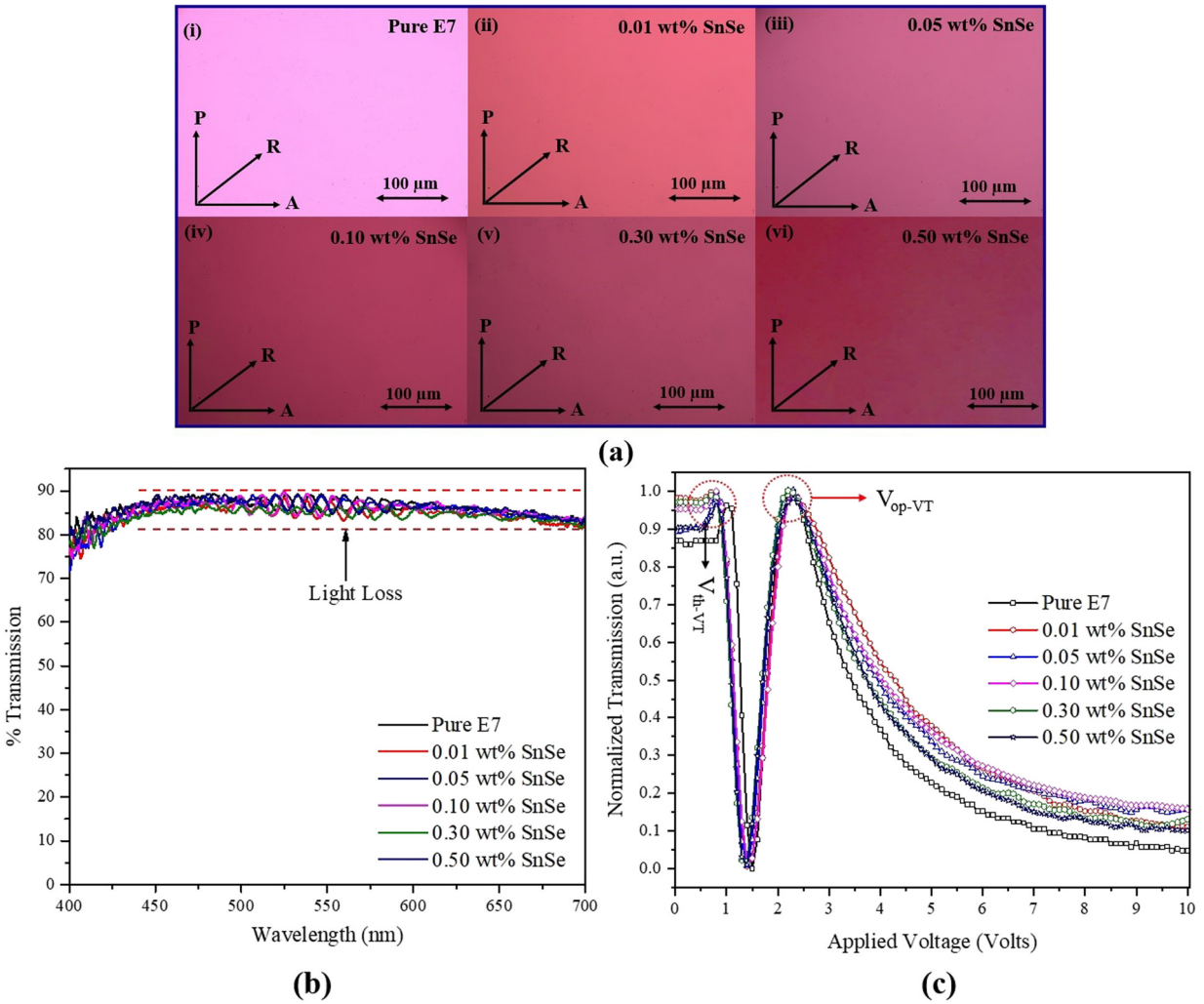

Fig. 2 POM textures in the bright state (a) (P, R and A represents the polarizer, analyser and rubbing direction of LC cells), transmission spectrum (b) and V–T curve (at f = 1 kHz) (c) of pure E7 and SnSe blended LC cells at RT.

Table 2 Estimated values of threshold voltage ($V_{th\text{-}VT}$ and $V_{th\text{-}POM}$), operating voltage (V_{op}), parallel ($\varepsilon'_{||}$) and perpendicular ($\varepsilon'_{\perp}$) component of dielectric permittivity, dielectric anisotropy ($\Delta\varepsilon$), splay elastic constant (K_{11}) at 1 kHz and room temperature (RT) and nematic–isotropic phase transition temperature (T_{NI}) measured by POM of pure and SnSe blended LC cells

SnSe NSs (wt%)	$V_{th\text{-}VT}$ (V)	$V_{th\text{-}POM}$ (V)	$V_{op\text{-}VT}$ (V)	$\varepsilon'_{||}$	$\varepsilon'_{\perp}$	$\Delta\varepsilon$	K_{11} (pN)	T_{NI} (°C)
Pure E7	1.08	1.10	2.30	18.94	4.67	14.27	15.11	61.50
0.01	1.02	1.10	2.29	20.66	4.59	16.07	15.07	61.50
0.05	0.95	1.00	2.25	21.66	4.55	17.11	13.74	61.00
0.10	0.90	0.95	2.23	22.59	4.51	18.08	13.20	61.00
0.30	0.83	0.85	2.20	23.30	4.48	18.82	11.69	61.00
0.50	0.73	0.75	2.20	23.95	4.45	19.50	9.38	60.50

The key distinction between these two methods relies on the capability of POM measurements to observe a precise orientation of the director at V_{th}, while the V–T curve technique primarily detects the initiation of the switching mechanism. This discrepancy arises due to the localized nature of V–T curve measurements, which are conducted on a small, isolated area, in contrast to POM data that are collected from the entire ITO electrode. Consequently, the threshold voltage values obtained from the POM investigations ($V_{th\text{-}POM}$) using the bias electric field tend to be exaggerated when compared to the results obtained from the V–T curve experiment ($V_{th\text{-}VT}$). Nevertheless, the precision of this approach is undermined by a finite experimental error method that we encountered while recording the transmitted light. In Fig. 2(c), it can be observed that $V_{th\text{-}VT}$ and $V_{th\text{-}POM}$ decreases by approximately 32.59% and 31.82%, respectively, for 0.5 wt% SnSe blended LC cells, attributed to a decrease in the ratio of the square root of splay elastic constant (K_{11}) and dielectric anisotropy ($\Delta\varepsilon$) (see Table 2) as illustrated in eqn (2).[45]

$$V_{th\text{-}VT} = \sqrt{\frac{K_{11}\pi^2}{\Delta\varepsilon\varepsilon_o}}, \quad (2)$$

The threshold voltage ($V_{th\text{-}VT}$) can be determined by analyzing the V–T curve, and the dielectric anisotropy ($\Delta\varepsilon$) of the SnSe composite can be obtained. These parameters allow for

calculation of the splay elastic constants (K_{11}) using eqn (2). The splay elastic constant is a significant parameter that characterizes the elastic interaction among nematic molecules in the LC material. Importantly, in the presence of SnSe NSs within the LC, the value of K_{11} for the E7-SnSe composites provides insights not only into the interaction between LC molecules but also between LC molecules and SnSe NSs themselves. The concentration dependence of K_{11}, as observed in Table 2, corresponds to the threshold voltage behaviour exhibited by the E7-SnSe suspensions. Incorporating a minute amount (0.5 wt%) of SnSe NSs results in significant improvements in the material properties. With increasing SnSe concentration (>0.5 wt%), the structural regularity decreases, and the composite exhibits a greater number of defects, rendering it more susceptible to reorientation. Moreover, the aggregation of SnSe disrupts the director field within the composite.

To evaluate the influence of SnSe NSs dispersion within pure E7 NLC, it is crucial to analyze alterations in both the physical and electro-optical characteristics of the NLC subsequent to the introduction of NSs. In this context, polarized optical microscopy (POM) measurements were carried out to ascertain the nematic–isotropic transition temperatures (T_{NI}) for E7/NSs composites, and the results are outlined in Table 2. Interestingly, the T_{NI} values remained almost identical across the concentration range between 61.5 to 60.5 °C. Therefore, the POM observations indicate the occurrence of minor molecular disordering in the nematic phase with increasing SnSe NSs concentrations.

3.1 Electrode polarisation

Electrode polarization (EP) in LC cells occurs when charge carriers drift towards the appositively charged interfaces in the presence of an externally applied electric field with low-frequency. This investigation investigates a significant phenomenon driving the creation of regions with space charges in close proximity to the electrodes, thereby substantially enhancing the permittivity of the LC cell. When subjected to high-frequency driving, the swift alteration in the polarity of the external field surpasses the responsiveness of mobile charge carriers, impeding the development of space charges. This shift from behavior at high frequencies to that at low frequencies is clearly evident through a gradual shift in the real part of the permittivity ($\varepsilon'_{\perp}$) and a distinctive peak in the imaginary part ($\varepsilon''_{\perp}$) – a phenomenon recognized as Debye-type relaxation (see the relaxation frequency of flip-flop motion section of the ESI†).

Fig. 3 illustrates the complex permittivity ($\varepsilon^* = \varepsilon' + i\varepsilon''$) and the dielectric loss tangent ($\tan\delta = \varepsilon''/\varepsilon'$) of a dispersion containing 0.5 wt% SnSe in the pure E7 LC. The observed significant increase in the dielectric constant (ε') cannot be attributed to either the molecular dielectric relaxation or the influence on the nematic order by NSs. However, it is correlated with a heightened quantity of mobile charge carriers that respond to the external field, resulting in the accumulation of charges at the interfaces. As a consequence, the observed elevation in permittivity exhibits the effective permittivity of the LC cell. This perspective considers the influence of accumulated charges at the interfaces, as

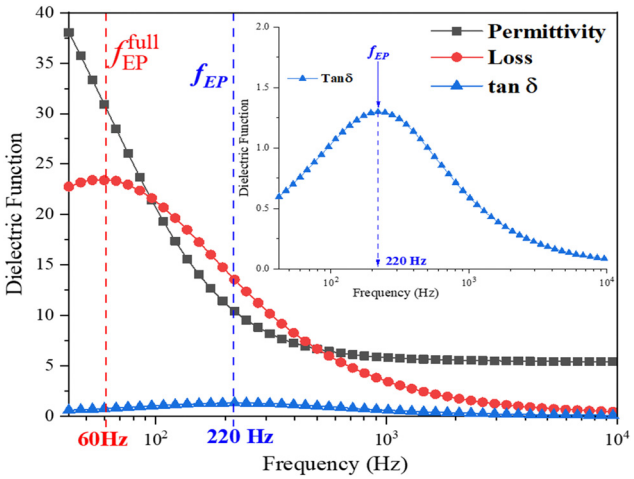

Fig. 3 Permittivity spectrum of a dispersion containing 0.5% SnSe nanospheres (NSs) in pure E7 LC, demonstrating the characteristics of dielectric permittivity components ($\varepsilon_{\perp}$ & $\varepsilon_{\parallel}$) and tan δ in the presence of electrode polarization (in HA mode). The initiation frequency of electrode polarization (f_{EP}) is determined by the peak value of tan delta, while the frequency at which it fully develops (f_{EP}^{full}) corresponds to the maximum dielectric loss. Furthermore, a substantial increase of more than two-fold is observed in the perpendicular component of dielectric permittivity within this range.

opposed to molecular relaxation processes occurring within the dielectric medium.

To clarify the mechanism of polarization within insulating controlled media, we employ a simplified model introduced by Coelho.[46,47] This model adequately reproduces the impedance characteristics in our specific case. As outlined in the Coelho model, the frequency at which EP initiates (f_{EP}) can be represented as follows:

$$f_{EP} = \frac{\sigma_o}{2\pi.\varepsilon_r\varepsilon_o}\sqrt{\frac{2\lambda_D}{d}} \quad (3)$$

The onset frequency (f_{EP}) is contingent on a range of factors, encompassing the conductivity (σ_o) and permittivity (ε_r) of the dielectric substance, the Debye screening length (λ_D), and the thickness (d) of the LC cell. At the onset frequency (f_{EP}), the electric loss tangent demonstrates its highest magnitude, denoting the peak of EP outcomes. Moreover, the real component of the LC cell's permittivity (ε') exceeds the low-frequency dielectric constant (ε_r) of the nematic host material.

Once fully developed, EP is distinguished by the presence of a prominent peak in the imaginary component of the permittivity (ε''). Below this frequency, the real part of the permittivity (ε') reaches a plateau, indicating a steady-state condition of electrode polarization. The inclusion of SnSe NSs in the dispersion enhances conductivity, shifting the onset frequency of f_{EP} to higher values compared to the pristine E7 LC system. The influence of the NSs on the electro-optical characteristics of the dispersion demonstrates variability contingent on whether the driving frequency surpasses or falls below the f_{EP}.

At frequencies lower than f_{EP}, where EP is not fully developed, the presence of NSs can have a different impact. This may include changes in the effective permittivity of the dispersion,

alterations in the charge accumulation at the interfaces, or modifications in the response to the external electric field. On the other hand, at frequencies higher than f_{EP}, where EP is fully developed, the influence of NSs may differ. This could involve changes in the dielectric properties, modifications in the dispersion's optical response, or other effects related to the interaction between the NSs and the electric field. In summary, the impact of SnSe NSs doping on the electro-optical performance of the dispersion is influenced by the driving frequency, with distinct effects observed below and above the onset frequency of EP, f_{EP}.

3.2 Impact on dielectric properties

In the realm of LC technologies, the operational frequencies for LC cells and displays frequently fall within the mid-range, typically ranging from 100 Hz to 10 kHz, marking the static operational domain. However, when frequencies fall below this range, a captivating flickering phenomenon emerges as a result of the dielectric reorientation of LC molecules in response to the applied electric field. On the contrary, elevated frequencies lead to a decline in performance, a consequence of heightened resistivity within connecting wires and ITO-electrodes, coupled with the manifestation of molecular dipole relaxations.

To comprehensively evaluate the dielectric and electro-optic performance of NLC, a prevailing practice is to explore the frequency range of 1–3 kHz. This specific frequency interval facilitates a thorough investigation of the influence of nanoparticle doping on the dielectric properties, while also considering the distinction between driving frequencies above the onset frequency of electrode polarization (f_{EP}) and those below, where electrode polarization remains active (see Fig. S2 to S5 in the ESI†). This study aims to shed light on the impact of nanoparticle doping on NLC's dielectric characteristics within the specified frequency range, advancing our understanding of LC devices' performance in practical applications.

When operating at frequencies above f_{EP} ($f > f_{EP}$), the fully developed EP can be influenced by NS doping. This can result in modified dielectric properties, optical response, and other aspects related to the interaction between the NSs and the electric field. At lower frequencies where EP is present but not fully developed, nanoparticle doping may also affect the electro-optical performance. This can involve changes in the effective permittivity of the dispersion, charge accumulation at the interfaces, and the response to the applied electric field. By considering the impact of nanoparticle doping at different driving frequencies, both above and below f_{EP}, a comprehensive understanding of the electro-optical behavior of a LC system can be gained. This knowledge is crucial for optimizing and enhancing the performance of LC-based devices.

Below the onset frequency f_{EP} ($f < f_{EP}$), the presence of space charges near the electrodes causes a substantial increase in permittivity, spanning a wide range of values. For the host E7 LC, the onset frequency for EP is larger for the VA cell (at f_{EP} 290 Hz; see Fig. S6 in ESI†) as compared to the HA cell (at f_{EP} = 220 Hz; see Inset of Fig. 3). As a result, the rise in permittivity ($\varepsilon_{\parallel}$) occurs at higher frequencies than that of the rise in permittivity ($\varepsilon_{\perp}$). Subsequently, two noteworthy effects can be discerned:

(i) In the frequency range between the onset frequencies f_{EP} for HA and VA LC cells, a notable increase in the dielectric anisotropy ($\Delta\varepsilon = \varepsilon_{\parallel} - \varepsilon_{\perp}$) becomes apparent. This increase is primarily attributed to the influence of EP on $\varepsilon_{\parallel}$ (where only $\varepsilon_{\parallel}$ is affected by EP). Similarly, when the frequency is below the f_{EP} in the HA and VA alignments, $\Delta\varepsilon$ appears to be amplified due to a more significant enhancement of $\varepsilon_{\parallel}$ than $\varepsilon_{\perp}$ (see Fig. S2 to S5 in the ESI†).

(ii) When comparing multiple samples featuring uniform alignment yet differing doping concentrations (yielding distinct conductivity levels), and when the frequency remains below the designated f_{EP} threshold for a minimum of one sample, a significant influence of NSs on permittivity becomes apparent. It is imperative to emphasize that these observations remain detached from the dipolar relaxation behaviors exhibited by LC molecules or fluctuations in the nematic order parameter. Rather, the emergence of space charges, driving these noteworthy effects.

In the case of thin LC cells possessing a thickness below 5 μm and exhibiting significant doping concentrations, the initiation frequency f_{EP} associated with electrode polarization could closely align with the conventional frequency benchmark of 1 kHz. In this scenario, we put forward the notion that elevating the frequency to higher magnitudes could yield insightful revelations in the comprehension of permittivity data within the realm of nanocomposites.

In Fig. 4(a), the variations in the parallel ($\varepsilon_{\parallel}$) and perpendicular ($\varepsilon_{\perp}$) components of dielectric permittivity are presented as a function of reduced temperature ($T - T_{NI}$) for both the pure E7 LCs and E7 LC doped with SnSe NSs, with measurements conducted at a standard frequency of 1 kHz, which falls above the onset frequency f_{EP} for electrode polarization in the static dielectric regime. The curve illustrates that, in comparison to the pure LC, the presence of different concentrations of SnSe NSs in the LC leads to a decrease in $\varepsilon_{\perp}$ and an increase in $\varepsilon_{\parallel}$. Notably, E7 is a compound known for its high polarity, and the introduction of guest NSs to this LC mixture can have a substantial impact on the intermolecular interactions within the LC medium. When a SnSe NS possesses notable polarizability properties, it can affect the overall polarizability of the LC molecules, leading to a rotation of the dipole axis caused by charge redistribution. Considering that SnSe NSs do not significantly influence the angle β (the angle between molecular axis and dipole moment), it can be inferred that the charge transfer between SnSe NSs and LC molecules should augment both permittivity values. The increase in polarizability is corroborated by the average permittivity value, which rises as the concentration of SnSe NSs increases, as shown in Fig. 4(b). However, a contrary tendency may be seen in the two permittivity values, where $\varepsilon_{\parallel}$ increases and $\varepsilon_{\perp}$ decreases with increasing NS concentration. However, a reduction in $\varepsilon_{\perp}$ corresponds to lowering the pretilt angle for the HA cell (see Fig. S7, S8 and Table S1, ESI†). Furthermore, previous studies have indicated that at lower concentrations of large-sized nanoparticles (NPs) in LCs, the effects of NPs are typically weak and do not significantly impact the dielectric permittivity.[48,49] Notably, in our study, we observed that both $\varepsilon_{\perp}$ and $\varepsilon_{\parallel}$ change significantly

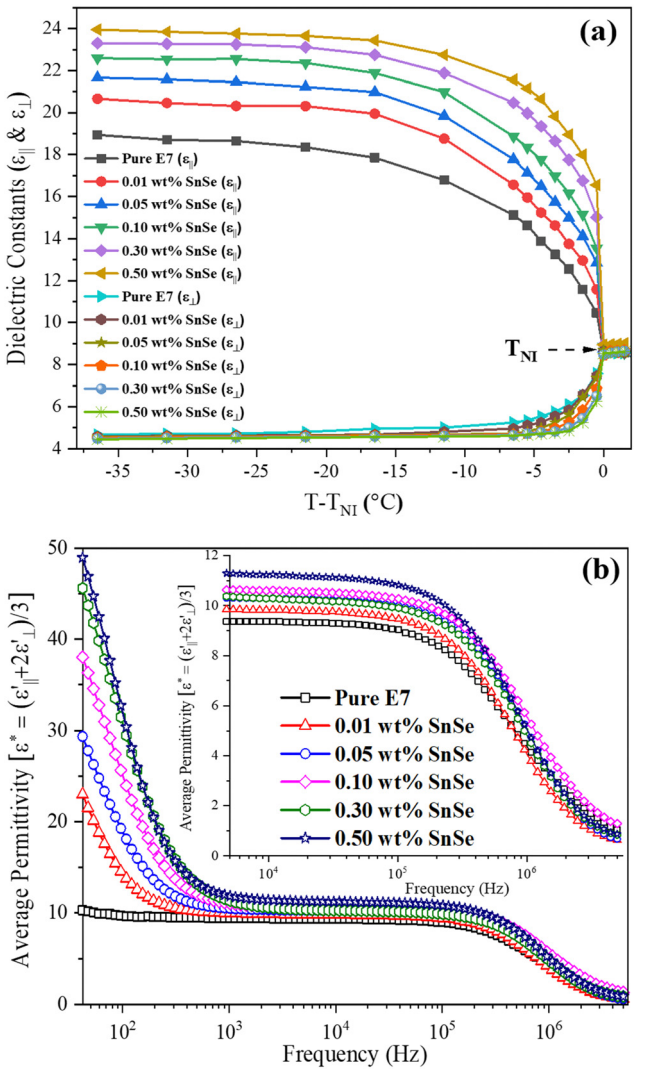

Fig. 4 (a) Variation of parallel and perpendicular components of the dielectric constant (at 1 kHz > f_{EP}) with reduced temperature for pure E7 and SnSe-blended LC cells, and (b) the average permittivity of LC cells at room temperature with various concentrations of SnSe nanospheres. The inset of (b) represents an enlarged view of the average permittivity from 5 kHz to 5.5 MHz.

(see Table 2) at very low concentrations (0.01 wt%) of SnSe NSs and this behavior remains alike up to 0.5 wt%.

In order to obtain a better understanding of the impact of dielectric anisotropy ($\Delta\varepsilon$) on the threshold voltage, we conducted calculations on the SnSe NSs-nematic composite. By examining the ratio of $\sqrt{\Delta\varepsilon^{LC+NSs}/\Delta\varepsilon^{LC}}$ for different concentrations of SnSe NSs (0.01, 0.05, 0.1, 0.3, and 0.5 wt%), we obtained values of 1.06, 1.09, 1.12, 1.15 and 1.17, respectively. Notably, these values closely align with the ratio of V_{th}, $\sqrt{V_{th}^{LC}/V_{th}^{LC+NPs}}$ = 1.03, 1.06, 1.10, 1.14 and 1.22. Our findings indicate that the decrease in V_{th} does not only correspond directly to the decrease in $\Delta\varepsilon$. This suggests that the addition of SnSe NSs in the nematic LC can significantly impact the K_{11}. However, we did observe a consistent monotonic decrease in the ratio of K_{11} to $\Delta\varepsilon$ as the concentration of NSs in the composites increases $\left(\sqrt{K_{11}/\Delta\varepsilon} = 1.03,\ 0.97,\ 0.90,\ 0.85,\ 0.79 \text{ and } 0.69\right)$. As a result, we can infer that the decrease in V_{th} for SnSe NSs-E7 composites is influenced jointly by the splay elastic constant and dielectric anisotropy.

3.3 Impact on threshold voltage

The threshold voltage (V_{th}) is a crucial parameter quantifying the interplay between electric torque, dielectric anisotropy-induced director field reorientation, and elastic torque due to bulk elasticity. V_{th} alterations from doping relate to changes in bulk elasticity or dielectric anisotropy. This is valid for driving frequencies exceeding f_{EP}, considering that the applied voltage and electric field have a linear correlation ($E = V/d$), where V is the voltage and d is the cell thickness. Electrode polarization introduces nonlinearity in an applied voltage-electric field relationship, reducing the electric field magnitude at the LC throughout the LC cell. Consequently, lower frequencies require significantly higher external voltage for director reorientation. This phenomenon is demonstrated in experiments utilizing SnSe NSs doped in E7 LC and filled in 5.2 μm LC cells (see Fig. 5).

The pristine E7, exhibits a frequency-independent V_{th} of 1.08 V at 300 K. However, when SnSe NSs are introduced as dopants, dispersions demonstrate a noticeable increase in V_{th} at lower frequencies. Nevertheless, at frequencies exceeding 200 Hz, the observed V_{th} value becomes constant for all higher frequencies like the pure host. It is worth noting that in practical applications of LC cells and LCDs, the cell gaps are often narrower than 5 μm (some are greater than 5 μm *i.e.*, between 5–10 μm). Consequently, the critical frequency at which this significant rise in threshold occurs is expected to shift towards higher frequencies, as predicted by eqn (3).

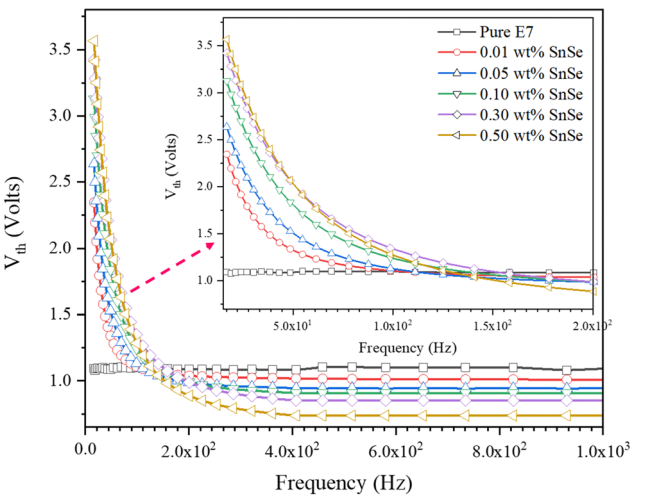

Fig. 5 The influence of electrode polarization on the threshold voltage. It demonstrates the frequency-dependent behaviour of the threshold voltage of SnSe blended LC cells at RT.

3.4. Impact on electro-optical response

This section focuses on investigating the dynamic responses of the pure E7 and SnSe blended LC cells. These responses can be characterized by two important response time parameters: τ_{rise} and τ_{decay}. τ_{rise} represents the time taken by the nematic director to orient from a homogeneous to a homeotropic configuration under an external applied voltage across a homogeneously-aligned (HA) LC cell. Similarly, τ_{decay} signifies the time required for the director to reorient from the homeotropic to the homogeneous configuration after the voltage is turned off. These parameters can be expressed mathematically using the following equations for strongly anchoring LC cells:[50,51]

$$\tau_{rise} = \frac{\gamma d^2}{(\Delta\varepsilon\varepsilon_o V^2 - \pi^2 K_{11})} \text{ and } \tau_{decay} = \frac{\gamma d^2}{\pi^2 K_{11}}, \quad (4)$$

Here, γ symbolizes the rotational viscosity of the liquid crystal, d corresponds to the thickness of the cell, ε_o stands for the permittivity of free space, K_{11} represents the splay elastic constant, and V denotes the externally applied voltage.

However, the primary factor influencing the dynamic response is the rotation of the nematic director upon the application or removal of an external electric field. So, by neglecting the backflow within the LC cell, one can establish a proportional relationship between them *i.e.*, $\tau_{rise} \propto \tau_{on}$ and $\tau_{decay} \propto \tau_{off}$.

Fig. 6(a) present the field-induced dynamic responses, specifically the τ_{on} and τ_{off}, of the pure E7 and SnSe NSs blended LC cells. Once a voltage exceeding the threshold switching voltage was introduced, an intricate and dynamic response was apparent within the system. To understand this behaviour, we employed an electro-optical configuration and processed the collected data using the LabView software platform. The rise and fall times, representing the durations for the transmission to transition from 90% to 10% and from 10% to 90% of the maximum transmission, respectively, are essential parameters for characterizing the system's performance.

The rise time primarily corresponds to the reorientation driven by electric torque, while the fall time relates to the free relaxation reorientation of nematic molecules. As a result, the rise time is generally much shorter than the fall time.

At room temperature (RT), we made interesting observations with NSs blended LC cells. Specifically, the characteristic times (τ_{on} and τ_{off}) decreased as we increased the concentrations of NSs. However, in the case of the SnSe NSs composite, the fall time exhibited a decrease with increasing concentrations due to a decrease in the rotational viscosity (γ) within the composite.

For SnSe blended LC cells, the τ_{on} experienced reductions of 2.22%, 7.78%, 11.11%, 13.33%, and 15.56% for 0.01, 0.05, 0.1, 0.3, and 0.5 wt% of SnSe NSs, respectively. Even more significantly, the τ_{off} showed greater reductions of 33.22%, 47.13%, 55.48%, 60.87%, and 63.68% for the corresponding concentrations of SnSe NSs. These findings highlight the influence of SnSe NSs on the dynamic response of the LC cells, presenting potential opportunities for tailoring their performance in practical applications.

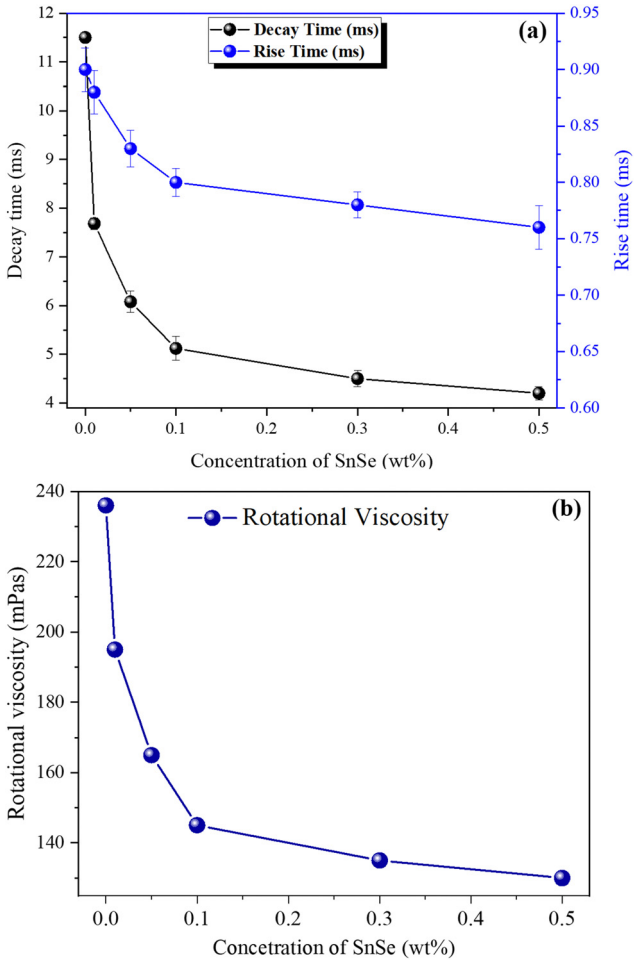

Fig. 6 Dynamic response time (a) and rotational viscosity (b) of pure and SnSe blended LC cells (~5.2 μm) at RT.

Fig. 6(b) depicts the rotational viscosity (γ) measurements of pure E7 and hybrid LC cells containing SnSe NSs. Notably, at room temperature, an observable trend emerged: as the concentration of SnSe NSs in the pure NLC increased, the γ exhibited a considerable reduction. Specifically, in the current study, the decrement in the γ value was quantified at 17.37%, 30.08%, 38.56%, 42.80%, and 44.91% for SnSe NSs concentrations of 0.01 wt%, 0.05 wt%, 0.1 wt%, 0.3 wt%, and 0.5 wt% in the LC cells, respectively. The reduction of γ can be explained by following three mechanisms:

The first effect is lubricating, which is caused by the huge size of SnSe NSs in comparison to the molecular size of the LC. The nanoparticles serve as physical spacers between the LC molecules, which reduces intermolecular interactions and friction. This results in a decrease in flow resistance and, as a result, a drop in viscosity. Second, the surface chemistry and characteristics of the SnSe NSs may encourage favourable interactions with the LC molecules. These interactions can change the ordering and alignment of the LCs, making molecular reorientation easier and lowering viscosity. Third, molecular structure disruption: The introduction of SnSe NSs can disturb the LC's regular molecular structure, particularly in

densely packed NSs regions. This disruption can reduce the strength of intermolecular forces, resulting in a lower viscosity. However, a decrease in T_{NI} indicates a decrease in the order parameter, although we only observed a minor decrease in T_{NI} (see Table 2).

According to eqn (4), under conditions of constant d and a fixed V, the response of the nematic director will be faster under the following conditions: reduced γ, increased $\Delta\varepsilon$, and decreased K_{11}. After evaluating the impact of these three aforementioned factors, it is evident that the reduction in response time cannot be solely attributed to them. This suggests the involvement of an additional factor that makes an additional contribution to the observed phenomenon. To provide a comprehensive explanation, we propose a model that takes into account this additional factor.

The operational dynamics of nematic liquid crystals (NLCs) under an applied voltage are outlined in Fig. 7(a), while Fig. 7(b) illustrates their behaviour in the absence of an applied voltage. The electro-optical enhancement observed in this study can be attributed to two mechanisms. First, by considering a semiconducting NSs in an electric field using the principles of electrodynamics. In this scenario, it's notable that the parallel component of the electric field acting on the NS becomes null, signifying the absence of any component along its surface. In contrast, the perpendicular component of the electric field at the NS surface equates to the surface charge density divided by the permittivity of the surrounding space. Consequently, within the NS, an electric field does not exist. This phenomenon finds mathematical expression through the following equation:[45]

$$E_{\perp} = \left(\frac{D_{\perp}}{\varepsilon}\right) = \left(\frac{\rho_{\text{Surface}}}{\varepsilon}\right) \quad (5)$$

where, $E_{\perp}$ denotes the component of electric field strength that is perpendicular to the surface, while $D_{\perp}$ represents the corresponding component of electric flux density in the same direction. The variable ε signifies the permittivity of the surrounding space, and ρ_{Surface} designates the density of surface charge at the interface.

The introduction of SnSe NSs induces changes in the surface charge density, leading to a significant impact on the electric field strength within the NLCs. As illustrated in Fig. 7(a), the inclusion of these semiconducting SnSe NSs alters the trajectory of the electric flux, resulting in its concentration around the surface of the SnSe NSs, situated between the top and bottom substrates. SnSe NSs have the ability to modulate the electric field lines. When these NSs are introduced into the LC system, they interact with the electric field and alter the field trajectory. This modification occurs due to the unique electrical properties of semiconducting materials, which enable them to influence the distribution and flow of electric flux. In the specific case of SnSe NSs, as shown in Fig. 7(a), their presence causes a deviation in the path of the electric flux, resulting in a concentration of the flux around the surface of the SnSe NSs. This alteration in the electric field path is a key factor in enhancing the overall electrical behaviour of the system. This concentration of electric flux intensifies the electric flux density and subsequently enhances the electric field strength in the vicinity of the SnSe NSs. Consequently, under the same applied voltage, the increased electric field strength causes the NLC molecules to respond rapidly, leading to the desired transmittance. Moreover, this phenomenon may also contribute to a lower threshold voltage and faster response time.

An additional mechanism that contributes to the enhanced performance is associated with the alleviation of the screening effect.[52] At the outset, ion impurities attach themselves to the alignment layer, maintaining their position until a voltage is introduced to the LC cell. The presence of these ion charges on the alignment layer stimulates an inherent direct current field within, leading to a decrease in the effective voltage encountered by the LC cell. However, the presence of SnSe NSs within the NLC molecules acts as a trap for these ions, as depicted in Fig. 7(a). This leads to a substantial reduction in impurity accumulation on the alignment layers, consequently diminishing the impact of the screen effect.

Typically, LCs contain a substantial concentration of free ions (impurity ions), thereby augmenting rotational viscosity by impeding the response of the nematic director to an external field. The introduction of SnSe NSs serves as a deterrent for ions possessing a high ion-trapping constant, leading to their entrapment at the adsorbing sites on SnSe NSs. Consequently, the incorporation of a judicious quantity of SnSe NSs into the LC medium results in a diminished concentration of free ions, concomitantly reducing rotational viscosity in the composites. The synergistic influence of heightened dielectric anisotropy and diminished rotational viscosity within the E7 LC/SnSe NSs composite system facilitates a swifter molecular response to an applied electric field. This attribute shows promise for the advancement of expeditious liquid crystal display (LCD) technology (see the Ion Trapping Mechanism section in the ESI†).

The enhancement in fall time, observed in the absence of applied voltages, can be attributed to the altered interaction between the LC molecules and the alignment layer due to the

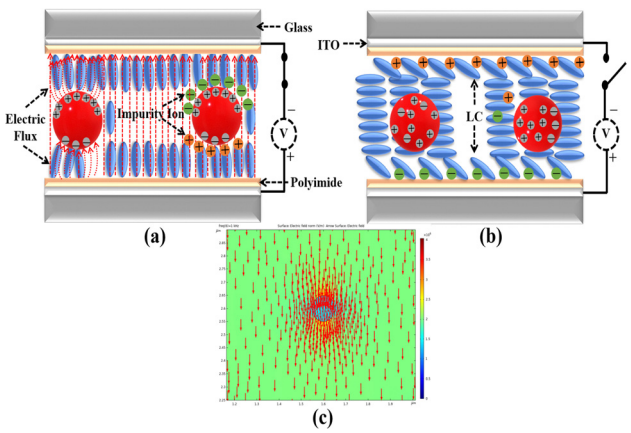

Fig. 7 (a) Schematic representation illustrating the functioning of NLCs in an on state NLC cell doped with SnSe NSs. (b) Schematic depiction illustrating the functioning of NLCs in an off state NLC cell doped with SnSe NSs and (c) the calculated distribution of an electric field in a NS surrounded by LC molecules. The electric field direction is indicated by the red arrow, while the color represents the field strength.

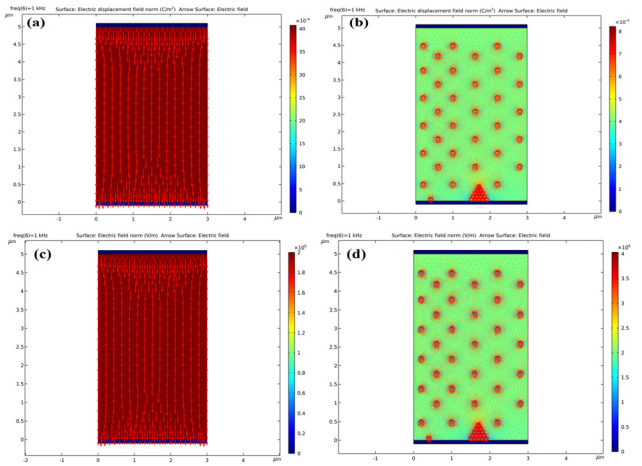

Fig. 8 Calculated distribution of electric flux density (a and b) and electric field (c) and (d) of pure E7 and SnSe blended LC Cell respectively. The electric field direction is indicated by the red arrow, while the color represents the field strength.

presence of SnSe NSs, as depicted in Fig. 7(b). When no voltage is applied, the SnSe NSs experience intermittent electrification caused by charged ionic impurities. These electrically charged SnSe NSs within the NLC molecules lead to a gathering of the charged ionic impurities around them, effectively separating them from the alignment layer. As a result, the force exerted by the alignment layer on the liquid crystal (LC) molecules intensifies, indicating a heightened level of van der Waals dispersion interactions between the NLC molecules and the alignment layers. This increased strength in van der Waals forces facilitates swift responses within the NLC molecules, even in situations where an external voltage is not applied. Fig. 7(c) illustrates the results obtained through the simulation *via* COMSOL Multiphysics (Version 6.1), a commercially available finite element software. The dielectric constants of the sphere and the surrounding medium were determined to be 4.22 and 4.75, respectively. It should be noted that the sphere was scaled up in the calculation to magnify the physical mechanism for demonstration purposes rather than representing its actual size. It indicates the dispersion of SnSe NSs in NLC significantly enhances the electric field of the LC-NS blended cell.

In summary, the inclusion of SnSe NSs imparts notable benefits, including a reduced threshold voltage, improved dielectric permittivity, and accelerated response of LC molecules, facilitated by two primary mechanisms: the interaction between LC molecules and the alignment layer, and the reinforcement of van der Waals dispersion interactions. These mechanisms collectively account for the observed improvements. To investigate the boundary conditions of the semiconductor within an electric field, we conducted simulations using the commercially available finite element software COMSOL Multiphysics simulation platform to model the behavior of SnSe NSs and NLC. The default material properties were assigned to the polyimide (PI) substrate, electrodes, E7 LC and SnSe NSs.

Fig. 8 provides simulated alterations observed in the electric field when subjected to applied voltages. In Fig. 8(a) and (b), notable shifts in the electric flux density around the SnSe NSs are evident. In contrast, the region without SnSe NSs shows no significant change in electric flux density. Additionally, Fig. 8(c) and (d) illustrate that the electric field aligns itself in the same orientation as the electric flux density, exhibiting increased strength compared to the region lacking SnSe NSs. Through a comparison of our experimental results with the outcomes of software simulations, we have successfully validated the consistency with established physical theories. Consequently, our findings confirm that the operation of NLC molecules is indeed enhanced by a more robust electric field intensity.

IV. Conclusions

In conclusion, our study focused on the dielectric and electro-optical properties of E7 nematic LC doped with SnSe NSs. As the concentration of SnSe NSs is increased (0.5 wt%), we observed a lower threshold voltage, faster response times, and reduced pretilt angles, indicating an improved electro-optical behaviour of E7 LC. We demonstrated that the controlled dispersion of the NSs in NLC renders superior properties as compared to their pristine counterparts. Our investigations have also unveiled that the conductivity induced by the NSs instigates the emergence of electrode polarization at lower driving frequencies, consequently exerting a detrimental influence on the electro-optical performance. Specifically, remarkable influences of the NSs on both the threshold voltage and permittivity have been documented. These effects display distinct positive and negative consequences depending on whether the driving frequencies are situated above or below the frequency threshold that signifies the initiation of electrode polarization.

Our findings also suggest that the NSs-dispersion in the E7 LC might be leading to electrode polarization and deterioration of electro-optical performance. Comprehending the source of mobile charge carriers has significant importance in tailoring the synthesis of NSs and the blending strategies of composites to attain NS/LC composites characterized by diminished conductivity and superior electro-optical performance. Overall, our study demonstrates the potential of SnSe NSs to enhance the dielectric and electro-optical properties of LC-based devices through simple physical mixing and highlights the importance of managing conductivity-related issues for improved electro-optical switching in various LC applications.

Author contributions

Conceptualization, investigation, methodology, data curation and writing – original draft: B. P. Singh; software simulation: P. Mishra; formal analysis and funding acquisition: M. R. Hatshan; supervision, visualization and validation: D. P. Singh; writing – review & editing, resources, supervision and funding acquisition: S. J. Hwang.

Conflicts of interest

There are no conflicts to declare.

Acknowledgements

The authors would like to thank the National Science and Technology Council of Taiwan for financially supporting this research under contract: (NSTC 111-2221-E-239-010-MY3) and (NSTC 111-2811-E-239-001-MY3). The author M. R. Hatshan is grateful to Researchers Supporting Project number (RSP2023R222), King Saud University, Riyadh, Saudi Arabia, for the financial support. DPS is thankful to the ULCO for funding the BQR project.

References

1 I. Dierking, *Nanomaterials*, 2018, **8**, 453, DOI: **10.3390/nano8070453**.
2 A. L. Rodarte, C. Gray, L. Hirst and S. Ghosh, *Phys. Rev. B: Condens. Matter Mater. Phys.*, 2012, **85**, 035430.
3 A. L. Rodarte, R. J. Pandolfi, S. Ghosh and L. S. Hirst, *J. Mater. Chem. C*, 2013, **1**, 5527–5532.
4 J. Mirzaei, M. Reznikov and T. Hegmann, *J. Mater. Chem.*, 2012, **22**, 22350–22365.
5 B. P. Singh, S. Sikarwar, R. Manohar, A. Shah, D. P. Singh, J. Herman and K. K. Pandey, *J. Appl. Phys.*, 2022, **131**, 174102.
6 A. Mikułko, P. Arora, A. Glushchenko, A. Lapanik and W. Haase, *Europhys. Lett.*, 2009, **87**, 27009.
7 R. Basu and A. Garvey, *Appl. Phys. Lett.*, 2014, **105**, 151905.
8 A. R. Ibrahim, M. F. Khyasudeen, J. Husband, S. M. Alauddin, N. F. K. Aripin, T. S. Velayutham, A. Martinez-Felipe and O. K. Abou-Zied, *J. Phys. Chem. C*, 2021, **125**, 22472–22482.
9 D. P. Singh, T. Vimal, Y. J. Mange, M. C. Varia, T. Nann, K. Pandey, R. Manohar and R. Douali, *J. Appl. Phys.*, 2018, **123**, 034101.
10 X. Liu, H. Luo, C. Yan, Y. Liu, H. Luo, D. Zhang and S. Chen, *J. Mater. Chem. C*, 2022, **10**, 17757–17767.
11 H. Liu, Y. Tang, C. Wang, Z. Xu, C. Yang, T. Huang, F. Zhang, D. Wu and X. Feng, *Adv. Funct. Mater.*, 2017, **27**, 1606269.
12 Y. Xia, T. S. Mathis, M.-Q. Zhao, B. Anasori, A. Dang, Z. Zhou, H. Cho, Y. Gogotsi and S. Yang, *Nature*, 2018, **557**, 409–412.
13 R. Kempaiah, Y. Liu, Z. Nie and R. Basu, *Appl. Phys. Lett.*, 2016, **108**, 083105.
14 Y. Garbovskiy, *Liq. Cryst.*, 2017, **44**, 948–955.
15 E. A. P. v Heijst, S. E. T. t Huurne, J. A. H. P. Sol, G. W. Castellanos, M. Ramezani, S. Murai, M. G. Debije and J. G. Rivas, *J. Appl. Phys.*, 2022, **131**, 083101.
16 T. Kambe, S. Imaoka, M. Shimizu, R. Hosono, D. Yan, H. Taya, M. Katakura, H. Nakamura, S. Kubo, A. Shishido and K. Yamamoto, *Nat. Commun.*, 2022, **13**, 1037.
17 B. P. Singh, C. Y. Huang, D. P. Singh, P. Palani, B. Duponchel, M. Sah, R. Manohar and K. K. Pandey, *J. Mol. Liq.*, 2021, **325**, 115130.
18 R. Basu and D. Gess, *Phys. Rev. E*, 2023, **10**, 024705.
19 Y. Garbovskiy and I. Glushchenko, *Crystals*, 2015, **5**, 501–533.
20 A. Sharma, P. Malik and P. Kumar, *Integr. Ferroelectr.*, 2019, **202**, 52–66.
21 N. Pushpavathi, K. Sandhya and S. K. Prasad, *J. Mol. Liq.*, 2020, **302**, 112571.
22 Y. Shen and I. Dierking, *Appl. Sci.*, 2019, **9**, 2512.
23 M. Jaiswal, G. Srivastava, S. Mishra, P. Kumar Singh, R. Dhar and R. Dabrowski, *J. Mol. Liq.*, 2023, **383**, 122032.
24 C. J. Hsu, B. P. Singh, M. Antony, P. Selvaraj, R. Manohar and C. Y. Huang, *Opt. Express*, 2020, **28**, 22856–22866.
25 C. J. Hsu, B. P. Singh, P. Selvaraj, M. Antony, R. Manohar and C. Y. Huang, *Sci. Rep.*, 2021, **11**, 17349.
26 L. Jinqian, Y. Zhao, H. Gao, D. Wang, Z. Miao, H. Cao, Z. Yang and W. He, *Liq. Cryst.*, 2022, **49**, 29–38.
27 J. F. Algorri, B. Garcia-Camara, A. Garcia-Garcia, V. Urruchi and J. M. Sánchez-Pena, *J. Light Technol.*, 2015, **33**, 2451–2455.
28 T. Zhang, C. Zhong and J. Xu, *Jpn. J. Appl. Phys.*, 2009, **48**, 055002.
29 M. Kumar and S. Kumar, *Polym. J.*, 2017, **49**, 85–111.
30 Q. Liu, Y. Yuan and I. I. Smalyukh, *Nano Lett.*, 2014, **14**, 4071–4077.
31 R. Gnawali, A. Volk, H. Al-Ghezi and P. P. Banerjee, *International Workshop on Thin Films for Electronics, Electro-Optics, Energy and Sensors (Proc. SPIE)*, 2023, **12477**, 85–86.
32 Y. Garbovskiy and A. Glushchenko, *Nanomaterials*, 2017, **7**, 361.
33 B. P. Singh, S. Sikarwar, S. Agarwal, D. P. Singh, K. K. Pandey and R. Manohar, *ACS Omega*, 2023, **8**, 2315–2327.
34 D. R. Evans, G. Cook, V. Y. Reshetnyak, C. M. Liebig, S. A. Basun and P. P. Banerjee, *Photorefractive Organic Materials and Applications*, 2016, pp. 223–247.
35 C. Guillen, J. Montero and J. Herrero, *Phys. Status Solidi A*, 2011, **208**, 679–683.
36 M. A. Franzman, C. W. Schlenker, M. E. Thompson and R. L. Brutchey, *J. Am. Chem. Soc.*, 2010, **132**, 4060–4061.
37 A. Agarwal, M. Vashi, D. Lakshminarayana and N. Batra, *J. Mater. Sci.: Mater. Electron.*, 2000, **11**, 67–71.
38 W. J. Baumgardner, J. J. Choi, Y.-F. Lim and T. Hanrath, *J. Am. Chem. Soc.*, 2010, **132**, 9519–9521.
39 G. Duvjir, T. Min, T. Thi Ly, T. Kim, A.-T. Duong, S. Cho, S. Rhim, J. Lee and J. Kim, *Appl. Phys. Lett.*, 2017, **110**, 262106.
40 H. D. Nguyen, J. S. Kang, M. Li and Y. Hu, *Nanoscale*, 2019, **11**, 3129–3137.
41 B. P. Singh, S. Sikarwar, K. Agrahari, S. Tripathi, R. K. Gangwar, R. Manohar and K. K. Pandey, *J. Mol. Liq.*, 2021, **325**, 115172.
42 K. Yang, *J. Appl. Phys.*, 1988, **64**, 4780–4781.
43 X. Zhao, T. Li, Z. Tang, Y. Li, Y. Miao, H. Xing, M. Cai, X. Wang, X. Kong and W. Ye, *Liq. Cryst.*, 2021, **48**, 15–22.
44 Y. A. Nastishin, R. Polak, S. V. Shiyanovskii, V. Bodnar and O. Lavrentovich, *J. Appl. Phys.*, 1999, **86**, 4199–4213.
45 D.-K. Yang and S.-T. Wu, *Fundamentals of liquid crystal devices*, John Wiley & Sons, 2014.
46 R. Coelho, *J. Appl. Phys.*, 1983, **18**, 137–146.
47 R. Coelho, *J. Non-Cryst. Solids*, 1991, **131**, 1136–1139.
48 R. Uttam, S. Kumar and R. Dhar, *Phys. Rev. E*, 2020, **102**, 052702.
49 R. Vafaie, A. Vahedi, M. Zakerhamidi and H. Tajalli, *Liq. Cryst.*, 2021, **48**, 1417–1428.
50 E. Jakeman and E. Raynes, *Phys. Lett. A*, 1972, **39**, 69–70.
51 L. M. Blinov and V. G. Chigrinov, *Electrooptic effects in liquid crystal materials*, Springer Science & Business Media, 1996.
52 P.-S. Chen, C.-C. Huang, Y.-W. Liu and C.-Y. Chao, *Appl. Phys. Lett.*, 2007, **90**, 211111-1–211111-3.